LASER & PHOTONICS REVIEWS
www.lpr-journal.org

Thin-Film Lithium Niobate Modulators with Ultra-High Modulation Efficiency

Xiangyu Meng, Can Yuan, Xingran Cheng, Shuai Yuan, Chenglin Shang, An Pan, Zhicheng Qu, Xuanhao Wang, Jun Wang, Peijie Zhang, Chengcheng Gui, Jiang Tang, Chao Chen, Cheng Zeng,* and Jinsong Xia**

Thin-film lithium niobate (TFLN)-based electro-optic modulators have extensive applications in broadband optical communications due to their broad bandwidth, high extinction ratio, and low optical loss. However, compared with their silicon and indium-phosphide (InP)-based counterparts, TFLN exhibits lower modulation efficiency. Simultaneously achieving low driving voltage and a wide modulating bandwidth poses a significant challenge. To address this limitation, this paper proposes a transparent conductive oxide film into the device, resulting in an ultra-high modulation efficiency of 1.02 V cm. The fabricated composite electrode not only attains high modulation efficiency but also sustains a high electro-optic bandwidth, as evidenced by the 3 dB roll-off at 108 GHz and the transmission of PAM-4 signals at 224 Gbit s^{-1}. The fabricated device offers novel solutions for low-cost, high-performance modulators, thereby facilitating the downsizing of TFLN-based multichannel optical transmitter chips.

1. Introduction

High-speed, low half-wave-voltage electro-optic (EO) modulators are used to convert microwave electrical signals into light signals. Hence, they play vital roles in fiber-optic communication networks[1] and microwave photonics.[2] Lithium niobate (LN) is the preferred material for most commercial EO modulators owing to its high electro-optic coefficient (≈31 pm V^{-1}) and transparency at telecommunication wavelengths.[1] Traditional bulk LN modulators rely on titanium-in-diffusion or proton-exchange methods,[3,4] Their fabricated waveguides have a low refractive index contrast of ≈0.1, leading to weak optical confinement and large optical mode sizes and gaps between the electrodes, ultimately resulting in low EO efficiency.

Lithium niobate on insulator (LNOI), also referred to as thin-film lithium niobate (TFLN), presents a promising platform for the development of photonic integrated circuits. Upon dry-etching the LN layer, the refractive index contrast of LN ridge waveguides significantly increases (by ≈ 0.7) compared with waveguides on bulk LN,[5] resulting in a small mode size. This enhancement leads to a smaller bend radius, compact size, and enhanced integration capability. Consequently, numerous photonic devices have been successfully fabricated on the LNOI platform,[6–14] including EO modulators with low half-wave voltages and large bandwidths.[15–19]

For commercial applications, enhancing the modulation efficiency of LN modulators is crucial. Increased modulation efficiency is desirable as it results in a reduced driving voltage and lower power consumption. The spacing between modulation electrodes can be substantially reduced compared to bulk materials due to the strong confinement of the optical field by LNOI waveguides with a high refractive index contrast. The EO modulation efficiency of TFLN typically ranges from 1.7 to 2.2 V cm in the C-Band,[17–26] whereas it tends to be lower in the O-Band. A notable achievement of a high modulation efficiency of 1.41 V cm has been realized in the C-Band using a high-dielectric constant cladding in the TFLN platform.[27] However, this efficiency is still lower than that of silicon on an insulator (SOI) (1.35 V cm)[28] and indium-phosphide (InP) (0.6 V cm)[29] platforms. This lower efficiency results in a longer modulation arm in the TFLN modulator and a larger coverage area than that of silicon optical chips, posing challenges for commercial applications. Therefore, addressing these limitations is crucial.

Recently, successful demonstrations of single-wave 200 Gbps transmission using high-performance TFLN EO modulators have been achieved. However, compared to differentially driven silicon modulators, LNOI modulators with ground–signal–ground (GSG) electrodes do not offer significant advantages in terms of size, cost, and power consumption. To address these issues, enhancing the modulation efficiency of LNOI EO

X. Meng, C. Yuan, X. Cheng, S. Yuan, C. Shang, A. Pan, Z. Qu, X. Wang, J. Wang, J. Tang, C. Chen, C. Zeng, J. Xia
Wuhan National Laboratory for Optoelectronics and School of Optical and Electronic Information
Huazhong University of Science and Technology
Wuhan, Hubei 430074, China
E-mail: cchen@hust.edu.cn; zengchengwuli@hust.edu.cn; jsxia@hust.edu.cn
P. Zhang, C. Gui
2012 Labs
Huawei Technologies Co., Ltd
Wuhan, Hubei 430079, China

The ORCID identification number(s) for the author(s) of this article can be found under https://doi.org/10.1002/lpor.202400809

DOI: 10.1002/lpor.202400809

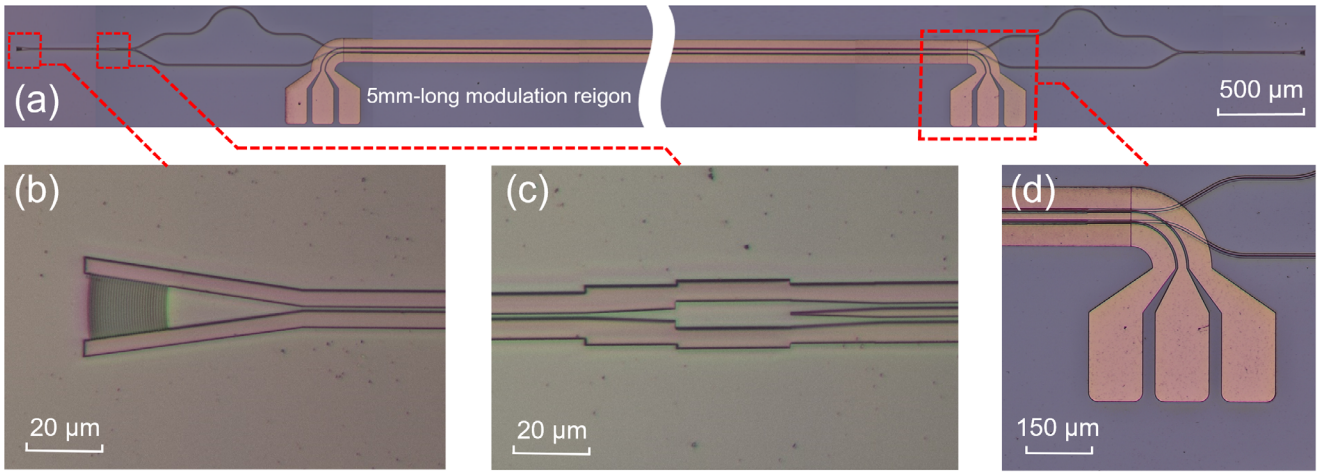

Figure 1. a) Overview of modulator under microscope. b) Grating coupler. c) Input multi-mode interference coupler. d) Terminal electrode pads.

modulators is imperative. Improved modulation efficiency will facilitate the development of small-sized array modulators with large bandwidths and low half-wave voltage. Consequently, this will further amplify the cost and power advantages of LNOI optical transmitter chips, advancing their future application in next-generation optical modules.

In this study, we introduced an ultrahigh-efficiency EO Mach–Zehnder modulator (MZM) on LNOI platform featuring a composite electrode composed of transparent conductive oxide (TCO) and gold. The absorption coefficient k of the TCO films was optimized to a low level of 0.001, resulting in a narrow composite electrode gap of 3 μm and a measured insertion loss of 2.9 dB. This design yielded a low half-wave-voltage length product of 1.02 V cm, marking the highest recorded value for the conventional MZM-type LNOI modulators. The proposed device exhibits a much wider optical bandwidth tolerance compared with existing solutions, such as slow-light EO modulators[30] and microcavity EO modulators.[31] In a 5 mm-long modulation region, we observed a 3-dB EO S21 roll-off at 108 GHz. Furthermore, we achieved successful implementations of 112 Gbit s^{-1} on–off keying (OOK) signal transmission and 224 Gbit s^{-1} signal transmission using four-level pulse amplitude modulation (PAM-4).

2. Results

Figure 1a illustrates an overview of the modulator. Two gratings were incorporated at both ends of the device to facilitate light coupling into and out of the chip for measurement, as shown in Figure 1b. The TE_0 mode light was coupled to the input grating, which was equally divided into two beams through the multi-mode interference (MMI) coupler (Figure 1c). Subsequently, the modulator was coupled to the same grating as the input. The TCO films were examined using scanning electron microscopy (SEM), as shown in Figure 4b. Figure 1d shows the terminal electrode pads. During testing, a 23 Ω terminal resistor was linked to the electrode pads via gold wire. The measured total insertion loss of the demonstrated modulator with a 3 μm TCO gap was 16.9 dB, while the on-chip propagation loss was 2.9 dB at 1310 nm, with each grating coupler contributing 7.0 dB of loss.

2.1. Modulation Efficiency and EO Bandwidth Performance

A 100 kHz sawtooth electric signal was applied to the electrodes to measure the half-wave voltage. All the measured devices featured a 5 mm-long modulation region. As shown in **Figure 2a**, the 5 mm-long modulator with a 3 μm TCO gap exhibited a half-wave voltage of 2.04 V. Consequently, the half-wave voltage length product, $V_{\pi^*}L$, was as low as 1.02 V cm. Remarkably, the additional insertion loss induced by the absorption of the combined TCO and gold electrodes remained minimal.

For bandwidth measurements, a GSG radio frequency (RF) probe was employed to administer microwave signals to the electrodes. Microwave transmission S21 and reflection S11 were gauged using a vector network analyzer (Agilent N5227A, VNA). S21 was simulated by utilizing the CST studio suite solver (SIMULIA), as shown in Figure 2b. We evaluated the performance of the 5 mm-long modulation arm device. We observed that the EO S21 response rolled down to −3 dB at 108 GHz, showcasing impressive bandwidth performance. Additionally, the simulation results closely aligned with the test results.

2.2. Eye Diagram and Bit-Error Rate (BER) Performance

During testing, a 70 GHz arbitrary waveform generator (Keysight M8199A) was utilized to generate the data, which were amplified by a driver (SHF S804B) with an amplification factor of 22 dB and connected to the modulator. The output signal was measured using a 110 GHz sampling oscilloscope (Keysight N1000A) to record the eye diagram. A series of tests were conducted to further verify the performance of the TCO electrode modulator for high-speed data transmission. First, we assessed the eye diagram and BER of the modulator with a modulation area length of 5 mm. The optical eye diagrams of the OOK modulation at various modulation rates (56, 80, and 112 Gbit s^{-1}) on a 5 mm device are shown in **Figure 3a–c**. Additionally, we examined the PAM4 signal at rates of 112 and 224 Gbit s^{-1} (56, 112 GBaud), as shown in Figure 3d,e. To further gauge the back-to-back (B2B) BERs, we utilized an adjustable optical attenuator (Joinwit JW8507), a 90 GHz bandwidth optical detector (FINISAR XPDV4120R), and a

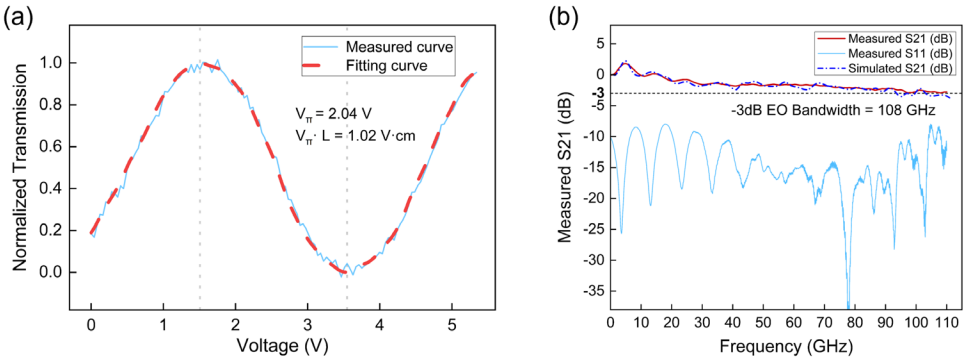

Figure 2. a) Normalized optical transmission of the 5 mm-long modulator with a 3 μm TCO gap as a function of the applied voltage. b) Electro-optic bandwidth performance of the 5 mm-long LN modulators.

70 GHz real-time oscilloscope (Keysight UXR0704A) to record the BER test data. The BER calculations were conducted offline using a MATLAB-based algorithm. The BER test results were assessed around the soft-decision forward error coding (SD-FEC) threshold (2×10^{-2}).

The results indicate that the dynamic extinction ratios of the eye diagrams for the 56 Gbit s^{-1} OOK to 224 Gbit s^{-1} PAM4 signals were (5.34, 4.15, 2.81, 2.32, and 1.98) dB, as shown in Figure 3a–e. We performed BER tests on the 112 Gbit s^{-1} OOK and PAM4 signals, as well as the 224 Gbit s^{-1} PAM4 signal, as illustrated in Figure 3f. Under the PAM4 signal transmitted at a high rate of 224 Gbit s^{-1}, the BER could be reduced to below the hard decision forward error coding (HD-FEC) threshold (3.8×10^{-3}) when the received optical power exceeded −13 dBm.

3. Discussion

In this study, we introduced an indium tin oxide (ITO) film into the electrode to enhance the modulation efficiency of the LNOI

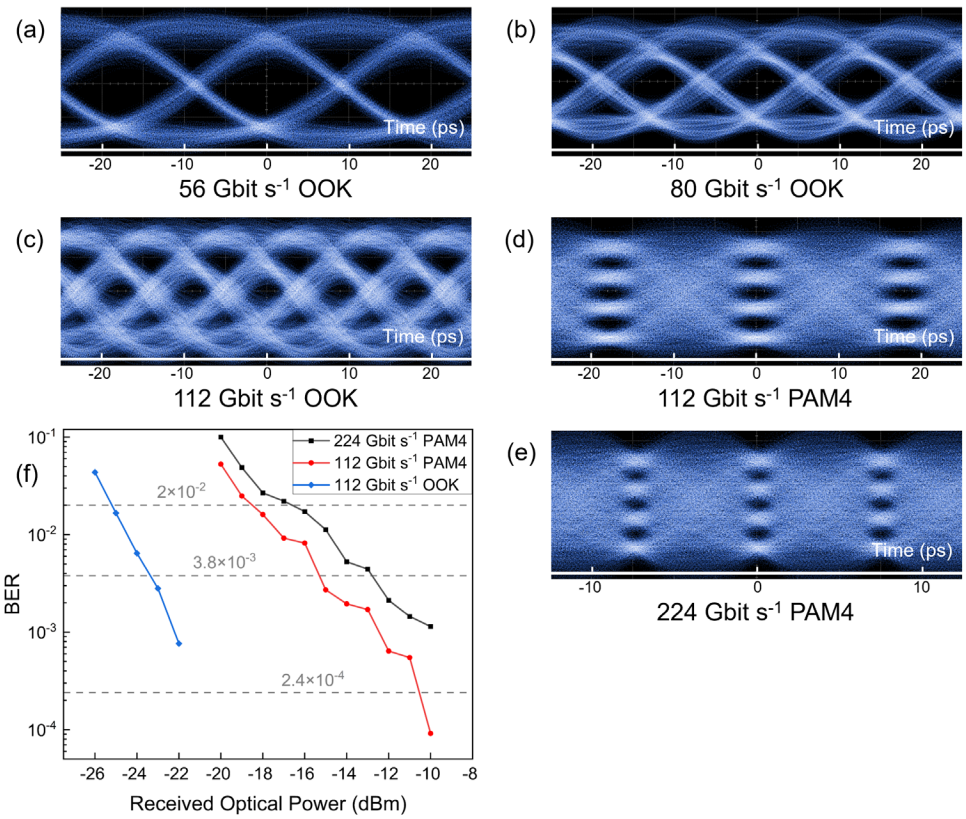

Figure 3. High-speed eye diagrams and bit-error test results of 5 mm devices. OOK format: a) 56 Gbit s^{-1}, b) 80 Gbit s^{-1}, c) 112 Gbit s^{-1}. PAM4 format: d) 112 Gbit s^{-1} (56 GBaud), e) 224 Gbit s^{-1} (112 GBaud). f) B2B BER test results of 112 Gbit s^{-1} OOK, 112 Gbit s^{-1} PAM4, and 224 Gbit s^{-1} PAM4 measured under receiving power.

Table 1. Comparison of device performance from different references.

Year	Working Band	$V_\pi L$ (V cm)	IL (dB)	BW (GHz)	References.
2018	C-Band	2.2	<0.5	100	[19]
2019	C-Band	2.2	2.5	>70	[18]
2020	O-Band	2	16	/	[34]
2020	C-Band	2.47	1.8	>67	[21]
2021	C-Band	1.7	17	>67	[17]
2021	C-Band	1.75	0.7 cm^{-1}	>40	[22]
2021	C-Band	2.3 ± 0.2	1 ± 0.5	>50	[24]
2022	C-Band	2.35	6.5 ± 0.5	110	[25]
2022	C-Band	2.2	0.2	>67	[26]
2023	C-Band	1.41	0.5	>40	[27]
2023	O-Band	1.85	2.5	65	[35]
2024	O-Band	1.02	2.9	108	This work

modulator while preserving its high modulation bandwidth. In comparison with the high modulation efficiency achieved by both the resonant cavity structure[31,32] and the slow-light structure,[30,33] the developed modulator is a conventional Mach–Zehnder interferometer (MZI) structure. Our modulator can accommodate broadband light input. Furthermore, based on our simulations, we determined that the modulation efficiency of our device operates in the C-Band, which utilizes the same electrode structure design, is ≈1.18 V cm. However, during the measurement, we observed that the eye diagram extinction ratio of the modulator was not high. This may be attributed to the impedance mismatch and the quality of gold and TCO electrodes. The insufficient conductivity of the gold electrode and the presence of rough sidewalls that resulted from the etching process of the TCO electrodes can introduce additional microwave losses, impacting the quality of the eye diagram. Nevertheless, the addition of the TCO material to the electrode improved the eye diagram extinction ratio by ≈4.7 dB (as shown in a comparison of Figure S6 in the Supporting Information).

Studies have reported that new materials or device structures can be applied to LNOI modulators by introducing SiO_2 buffer layers[16] and high-dielectric cladding materials.[27] We compared current devices with other advanced devices to evaluate their performance, as shown in **Table 1**, focusing on modulation efficiency, modulation bandwidth, and insertion loss. As summarized in Table 1, our device achieved the highest modulation efficiency while maintaining a large modulation bandwidth with an acceptable insertion loss.

TFLN EO modulator chips incorporating TCO electrodes represent a breakthrough in high modulation efficiency, resulting in a 40% reduction in chip length compared to conventional gold electrode modulator chips while maintaining the same half-wave voltage requirement. This abbreviated phase-shift region contributes to lower microwave losses and a broader EO modulation bandwidth. Consequently, an approximate 70% increase in chip yield and a significant reduction in the cost of a single chip are anticipated if our TCO electrode technology is implemented in TFLN multichannel optical transmitters in the future. This technology exhibits promising application prospects in data center optical modules and other pertinent areas. Importantly, our proposed method presents a novel approach for enhancing TFLN modulators, offering valuable insights into improving modulation efficiency and expanding bandwidth. This represents a significant advancement in the field and holds promising potential for future developments.

In summary, we proposed a new type of modulator based on the LNOI platform, utilizing combined electrodes comprising TCO and gold to achieve high EO modulation efficiency. The electrode spacing is 3 μm, with an optical insertion loss of 2.9 dB attributed to a 100 nm buffer layer. Consequently, the modulator achieves an impressively low half-wave voltage length product of 1.02 V cm. Moreover, the 5 mm-long modulation region exhibits an EO 3 dB transmission roll-off at 108 GHz. Successful demonstrations of OOK modulation at 112 Gbit s^{-1} and four-level pulse amplitude modulation (PAM-4) at 224 Gbit s^{-1} are also presented. If applied to ITO composite electrodes, the proposed thin-film lithium niobate modulator can potentially significantly reduce the cost and power consumption of TFLN-based data center optical modules and short-distance coherent transmission modules.

4. Experimental Section

Design Principles: For an X-cut LN-based modulator, the quasi-DC half-wave-voltage length product $V_{\pi^*}L$ can be expressed as

$$V_{\pi^*}L = \frac{\lambda g}{{n_e}^3 \gamma_{33} \Gamma} \quad (1)$$

where L is the length of the modulation region, λ is the wavelength of the input light, n_e is the extraordinary optical refractive index of the LN crystal (2.177 at 1310 nm), γ_{33} is the EO coefficient of LN, Γ is the overlap integral between optical modes and the electrical field, and g is the gap between the electrodes. As shown in Equation (1), reducing the gap g proves to be an effective method for achieving high EO efficiency or a low $V_{\pi^*}L$. However, narrowing the electrode gap can lead to significant optical absorption loss. For traditional bulk LN platforms, fabricating electrodes on an optically transparent buffer layer such as silica is a common approach to mitigate optical loss. An experiment conducted on a TFLN platform, where a 100 nm-thick silica buffer layer was inserted between the LN waveguide and electrodes, successfully demonstrated

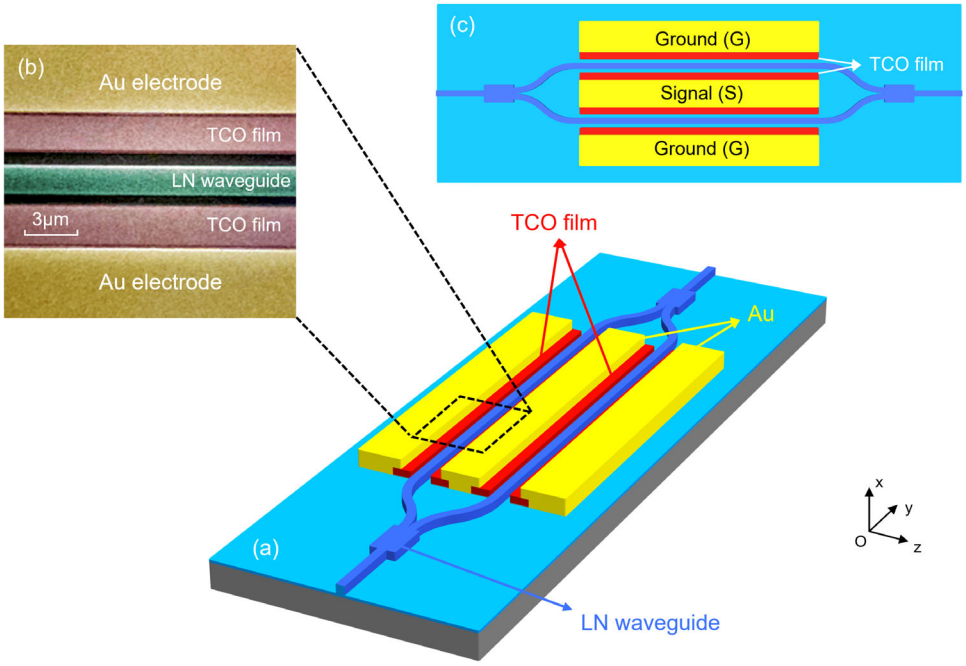

Figure 4. a) 3D schematic of the modulator, b) false color SEM of the combined electrodes and waveguides, and c) top view of the modulator.

a modulator with a half-wave-voltage length product of only 1.7 in the C-Band, utilizing a 3 μm electrode gap.[16]

A novel low-loss electrode type was required to further reduce the size of the modulator and enhance its bandwidth. TCO materials possess superior optical transparency and adjustable conductivity and had been employed in EO modulators of various material platforms.[36–40] By tuning the carrier concentration and mobility of the TCO material, a composite electrode could be formed by combining it with a gold electrode. This composite electrode could be positioned closer to the waveguide without causing heightened optical loss, which was advantageous for achieving higher EO efficiency. By adjusting cladding and buffer layer thicknesses, a microwave refractive index close to the light group index was achieved, facilitating velocity matching and resulting in higher EO bandwidth.[41] This could be realized through a specific structural design. Moreover, maintaining the advantage of a high bandwidth is possible by integrating traveling wave electrodes into the system.

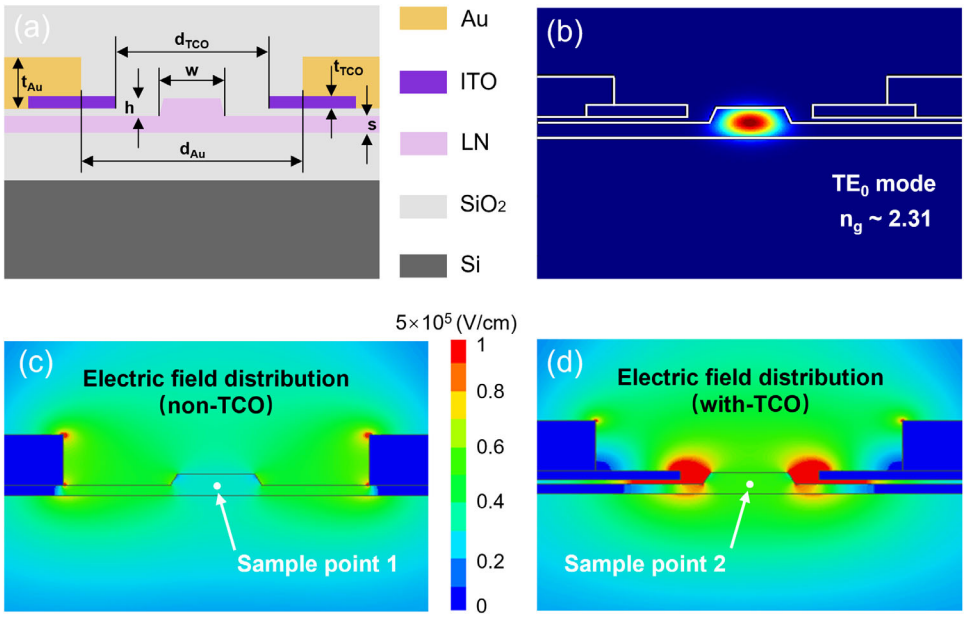

Figure 5. a) Cross-section of the phase modulator. b) Optical mode in LNOI waveguides with combined electrodes. Comparing the electric field with the same drive voltage (1 V) in c) a regular LNOI modulator with a 5 μm electrode gap and d) an LNOI waveguide with narrow gap combined electrodes (the gap between gold electrodes was 5 μm and the gap between ITO electrodes was 3 μm).

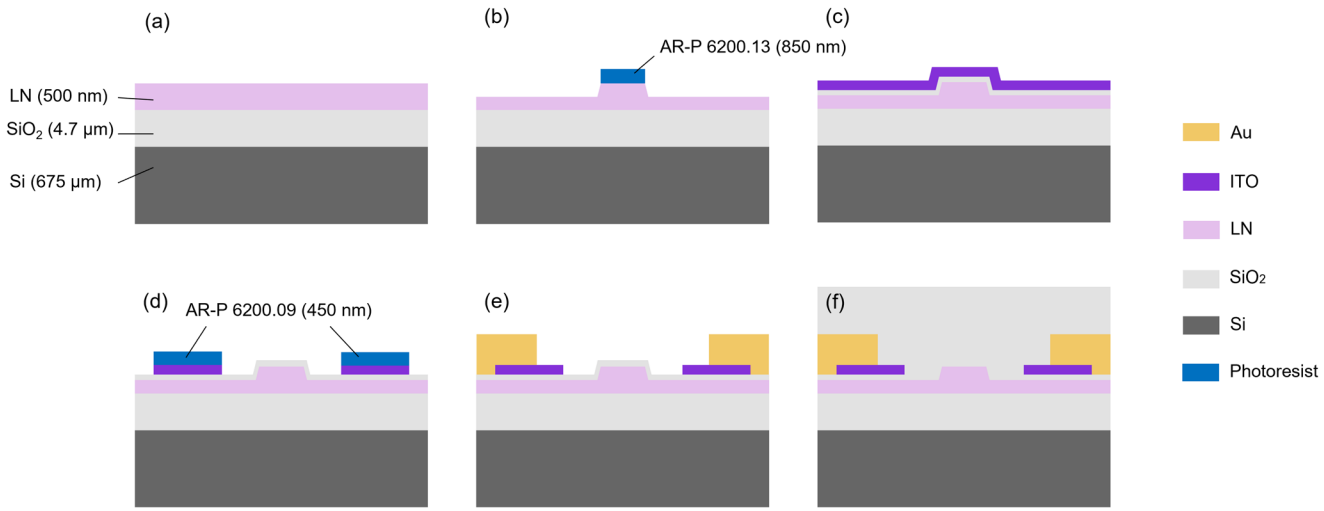

Figure 6. Outline of the fabrication process for the TCO-combined electrodes modulator. Photoresists include AR-P 6200.13 and AR-P 6200.09.

Design of TFLN Modulator with TCO Composite Electrode: The schematic structures of the fabricated modulator are shown in **Figures 4a** and 1a. Two 3 dB MMI couplers were utilized to divide the input light. Then, post-modulation was combined. A GSG electrode structure was employed in a push–pull modulation manner to reduce V_π. The conductivity of TCO materials (10^2–10^5 S m^{-1}) is significantly lower than that of gold ($\approx 10^8$ S m^{-1}). According to the simulations, replacing gold with a TCO material was not advantageous due to the degradation of microwave performance at high frequencies. Therefore, TCO and gold were combined as the traveling microwave electrodes to narrow the electrode gap without compromising the quality of RF signal transmission. Figure 4b illustrates a partially enlarged SEM image of the combined electrodes.

ITO was one of the several proposed TCO materials suitable for application on the LNOI platform. With its considerably lower refractive index than LN (1.5, measured at 1310 nm), ITO does not disrupt the optical modes in the waveguides. The values of the imaginary parts of the refractive index at 1,310 nm (0.0011) and the conductivity (8.05×10^5 S m^{-1}) were measured in testing (further details are presented in the Supporting Information). **Figure 5** presents the optical and electrical modes in one arm of the phase modulator (MZM). In the modulator segment of the ridge waveguide, the ridge height (h) was 260 nm, the width (w) was 2 μm, and the thickness (s) of the slab was 240 nm. The TCO-loaded composite electrode was situated on a 100 nm-thick silicon oxide buffer. The gold and TCO electrodes had spacings (d_{Au}) and (d_{TCO}) of 5 and 3 μm, respectively. The thicknesses of the gold (t_{Au}) and TCO (t_{TCO}) electrodes measured 1.4 μm and 180 nm, respectively. Figure 5b shows the tightly confined optical mode in the waveguides with a narrow gap between the ITO electrodes. Consequently, the electric field applied to the optical mode significantly increased. Figure 5c,d show the electric field distributions of the conventional modulator without TCO assistance and the modulator designed with TCO assistance, respectively. A sample point was selected at the center of the waveguide to further underscore the substantial enhancement in electric field intensity facilitated by the designed modulator. The simulation results reveal that by incorporating TCO materials to aid in electric field conduction, the electric field intensity at the central sample point of the two waveguides increased from 1.88×10^5 to 3.07×10^5 V m^{-1}. The contribution of TCO materials to facilitating electric field conduction was substantial.

Fabrication Process: An X-cut TFLN wafer from NanoLN, comprising a 500 nm LN film and 4.7 μm buried oxide layer, was utilized in this study. The fabrication process of the TCO-combined electrodes modulator shown in **Figure 6** was implemented based on this wafer. The fabrication process is as follows:

(a), (b) The waveguide pattern was transferred to the photoresist (AR-P 6200.13) using electron beam lithography (EBL) and etched in an inductively coupled plasma (ICP) with Ar.
(c) A layer of SiO_2 was deposited as a buffer layer on the etched TFLN waveguide, followed by the deposition of the ITO film.
(d) The ITO electrode patterns were then transferred to the photoresist (AR-P 6200.09) mask using EBL, and the etching process was conducted using ICP.
(e) Gold electrodes were deposited on the fabricated ITO electrodes through a lift-off process.
(f) Finally, a layer of SiO_2 was grown as cladding to complete the fabrication process.

Supporting Information

Supporting Information is available from the Wiley Online Library or from the author.

Acknowledgements

This work was supported by the National Key Research and Development Program of China (2022YFB2802402), the Natural Science Foundation of Hubei Province (2020CFA004), and the National Natural Science Foundation of China under Grant Nos. 62175079 and 62205119. The authors thank the Center of Micro-Fabrication and Characterization (CMFC) of WNLO and the Center for Nanoscale Characterization & Devices (CNCD), WNLO of HUST for the facility support.

Conflict of Interest

The authors declare no conflict of interest.

Author Contributions

X.M. and C.Y. contributed equally to this work. J.X., C.Z., C.C., and C.G. initiated the project and conceived the original idea with X.M., C.Y., and X.C.; X.M., X.C., C.S., and P.Z. designed the modulator structure and performed the numerical simulations; C.Y. and J.W. prepared and fabricated the ITO material; X.M., X.C., S.Y., and A.P. fabricated the full device; X.M., X.C., C.S., and X.W. tested the optical and microwave performances of the device; J.T., Z.Q., and P.Z. performed data analysis.

Data Availability Statement

The data that support the findings of this study are available from the corresponding author upon reasonable request.

Keywords

electro-optic modulator, high bandwidth, thin-film lithium niobate, transparent conductive oxide, ultra-high modulation efficiency

Received: May 31, 2024
Revised: August 13, 2024
Published online:

[1] E. L. Wooten, K. M. Kissa, A. Yi-Yan, E. J. Murphy, D. A. Lafaw, P. F. Hallemeier, D. Maack, D. V. Attanasio, D. J. Fritz, G. J. McBrien, *IEEE J. Sel. Top. Quantum Electron.* **2000**, *6*, 69.
[2] J. Capmany, D. Novak, *Nat. Photonics* **2007**, *1*, 319.
[3] L. Cai, Y. Kang, H. Hu, *Opt. Express* **2016**, *24*, 4640.
[4] H. Sato, K. Yamamoto, S. Yokoyama, in *2015 20th Microoptics Conference (MOC)*. (IEEE), New York 1.
[5] G. Poberaj, H. Hu, W. Sohler, P. Guenter, *Laser Photonics Rev.* **2012**, *6*, 488.
[6] C. Hu, A. Pan, T. Li, X. Wang, Y. Liu, S. Tao, C. Zeng, J. Xia, *Opt. Express* **2021**, *29*, 5397.
[7] J. Zhao, C. Ma, M. Rüsing, S. Mookherjea, *Phys. Rev. Lett.* **2020**, *124*, 163603.
[8] A. Pan, C. Hu, C. Zeng, J. Xia, *Opt. Express* **2019**, *27*, 35659.
[9] A. Boes, B. Corcoran, L. Chang, J. Bowers, A. Mitchell, *Laser Photonics Rev.* **2018**, *12*, 1700256.
[10] M. Zhang, C. Wang, R. Cheng, A. Shams-Ansari, M. Lončar, *Optica* **2017**, *4*, 1536.
[11] H. Liang, R. Luo, Y. He, H. Jiang, Q. Lin, *Optica* **2017**, *4*, 1251.
[12] X. Wang, C. Shang, A. Pan, X. Cheng, T. Gui, S. Yuan, C. Gui, K. Zheng, P. Zhang, X. Song, *APL Photonics* **2022**, *7*, 076101.
[13] J. Wei, Z. Hu, M. Zhang, P. Li, Y. Wu, C. Zeng, M. Tang, J. Xia, *Opt. Express* **2022**, *30*, 30564.
[14] C. Li, P. Chen, J. Li, K. Chen, C. Guo, L. Liu, *Opt. Eng.* **2022**, *61*, 057101.
[15] X. Wang, A. Pan, T. Li, C. Zeng, J. Xia, *Opt. Express* **2021**, *29*, 38044.
[16] X. Liu, B. Xiong, C. Sun, J. Wang, Z. Hao, L. Wang, Y. Han, H. Li, J. Yu, Y. Luo, *Chin. Opt. Lett.* **2021**, *19*, 060016.
[17] P. Kharel, C. Reimer, K. Luke, L. He, M. Zhang, *Optica* **2021**, *8*, 357.
[18] M. He, M. Xu, Y. Ren, J. Jian, Z. Ruan, Y. Xu, S. Gao, S. Sun, X. Wen, L. Zhou, *Nat. Photonics* **2019**, *13*, 359.
[19] C. Wang, M. Zhang, X. Chen, M. Bertrand, A. Shams-Ansari, S. Chandrasekhar, P. Winzer, M. Lončar, *Nature* **2018**, *562*, 101.
[20] S. Sun, M. He, M. Xu, S. Gao, Z. Chen, X. Zhang, Z. Ruan, X. Wu, L. Zhou, L. Liu, *Photonics Res.* **2020**, *8*, 1958.
[21] M. Xu, M. He, H. Zhang, J. Jian, Y. Pan, X. Liu, L. Chen, X. Meng, H. Chen, Z. Li, X. Xiao, S. Yu, S. Yu, X. Cai, *Nat. Commun.* **2020**, *11*, 3911.
[22] X. Liu, B. Xiong, C. Sun, J. Wang, Z. Hao, L. Wang, Y. Han, H. Li, J. Yu, Y. Luo, *arXiv preprint arXiv:2103.03684*, **2021**.
[23] Y. Liu, H. Li, J. Liu, S. Tan, Q. Lu, W. Guo, *Opt. Express* **2021**, *29*, 6320.
[24] P. Ying, H. Tan, J. Zhang, M. He, M. Xu, X. Liu, R. Ge, Y. Zhu, C. Liu, X. Cai, *Opt. Lett.* **2021**, *46*, 1478.
[25] M. Xu, Y. Zhu, F. Pittalà, J. Tang, M. He, W. C. Ng, J. Wang, Z. Ruan, X. Tang, M. Kuschnerov, *Optica* **2022**, *9*, 61.
[26] G. Chen, K. Chen, R. Gan, Z. Ruan, Z. Wang, P. Huang, C. Lu, A. P. T. Lau, D. Dai, C. Guo, *APL Photonics* **2022**, *7*, 2.
[27] N. Chen, K. Lou, Y. Yu, X. He, T. Chu, *Laser Photonics Rev.* **2023**, *17*, 2200927.
[28] M. S. Alam, X. Li, M. Jacques, Z. Xing, A. Samani, E. El-Fiky, P.-C. Koh, D. V. Plant, *J. Lightwave Technol.* **2021**, *39*, 4270.
[29] Y. Ogiso, J. Ozaki, Y. Ueda, H. Wakita, M. Nagatani, H. Yamazaki, M. Nakamura, T. Kobayashi, S. Kanazawa, Y. Hashizume, *J. Lightwave Technol.* **2019**, *38*, 249.
[30] C. Han, M. Jin, Y. Tao, B. Shen, X. Wang, *Micromachines* **2022**, *13*, 400.
[31] B.-C. Pan, H.-X. Liu, H.-C. Xu, Y.-S. Huang, H. Li, Z.-J. Yu, L. Liu, Y.-C. Shi, D.-X. Dai, *Chip* **2022**, *1*, 100029.
[32] B. Pan, H. Cao, Y. Huang, Z. Wang, K. Chen, H. Li, Z. Yu, D. Dai, *Photonics Res.* **2022**, *10*, 697.
[33] G. Chen, H. Wang, B. Chen, Z. Ruan, C. Guo, K. Chen, L. Liu, *Nanophotonics* **2023**, *12*, 3603.
[34] S. Sun, M. He, S. Yu, X. Cai, in *CLEO: Science and Innovations. STh1F. 4* (Optica Publishing Group), Washington.
[35] H. Li, Y. Tang, Q. Chen, X. Dai, X. Li, M. Lu, Q. Lu, W. Guo, *J. Phys. D: Appl. Phys.* **2023**, *56*, 154001.
[36] G. Xu, J. Ma, Z. Liu, B. Liu, S.-T. Ho, P. Zhu, L. Wang, Y. Yang, T. J. Marks, J. Luo, in *Linear and Nonlinear Optics of Organic Materials V.* SPIE, Bellingham, Washington pp. 238-246.
[37] X. Qiu, X. Ruan, Y. Li, F. Zhang, *J. Lightwave Technol.* **2018**, *36*, 2563.
[38] M. Y. Abdelatty, M. M. Badr, M. A. Swillam, *J. Lightwave Technol.* **2018**, *36*, 4198.
[39] G. Sinatkas, A. Pitilakis, D. C. Zografopoulos, R. Beccherelli, E. E. Kriezis, *J. Appl. Phys.* **2017**, *121*, 2.
[40] J. Tang, S. Yang, A. Bhatranand, in *Conference on Lasers and Electro-Optics/Pacific Rim. TUP6_2*, (Optica Publishing Group), Washington.
[41] D. Zhu, L. Shao, M. Yu, R. Cheng, B. Desiatov, C. Xin, Y. Hu, J. Holzgrafe, S. Ghosh, A. Shams-Ansari, *Adv. Opt. Photon.* **2021**, *13*, 242.